J. Fluid Mech. (2011), *vol.* 686, *pp.* 218–238.
doi:10.1017/jfm.2011.324

The local and global stability of confined planar wakes at intermediate Reynolds number

M. P. Juniper[1]†, O. Tammisola[2] and F. Lundell[2]

[1] Department of Engineering, University of Cambridge, Trumpington Street, Cambridge CB2 1PZ, UK

[2] Linné Flow Centre, KTH Mechanics, Royal Institute of Technology, S-100 44 Stockholm, Sweden

(Received 21 February 2011; revised 4 July 2011; accepted 22 July 2011;
first published online 27 September 2011)

At high Reynolds numbers, wake flows become more globally unstable when they are confined within a duct or between two flat plates. At Reynolds numbers around 100, however, global analyses suggest that such flows become more stable when confined, while local analyses suggest that they become more unstable. The aim of this paper is to resolve this apparent contradiction by examining a set of obstacle-free wakes. In this theoretical and numerical study, we combine global and local stability analyses of planar wake flows at $Re = 100$ to determine the effect of confinement. We find that confinement acts in three ways: it modifies the length of the recirculation zone if one exists, it brings the boundary layers closer to the shear layers, and it can make the flow more locally absolutely unstable. Depending on the flow parameters, these effects work with or against each other to destabilize or stabilize the flow. In wake flows at $Re = 100$ with free-slip boundaries, flows are most globally unstable when the outer flows are 50 % wider than the half-width of the inner flow because the first and third effects work together. In wake flows at $Re = 100$ with no-slip boundaries, confinement has little overall effect when the flows are weakly confined because the first two effects work against the third. Confinement has a strong stabilizing effect, however, when the flows are strongly confined because all three effects work together. By combining local and global analyses, we have been able to isolate these three effects and resolve the apparent contradictions in previous work.

Key words: absolute/convective instability, shear layers, wakes

1. Introduction

In this theoretical and numerical paper, we describe the effect of confining a viscous planar wake between two flat plates at $Re = 100$. In particular, we examine how the destabilizing effect of confinement is influenced by the boundary layers that are generated by the confining walls. Unlike our previous analyses, this one combines a local stability analysis with a global stability analysis over a wide range of confinements and shear ratios. This provides more information than can be obtained with independent local and global analyses.

Confined wake flows are frequently found in industry and in model problems. Our previous research into the effect of confinement has been motivated partly by

† Email address for correspondence: mpj1001@cam.ac.uk

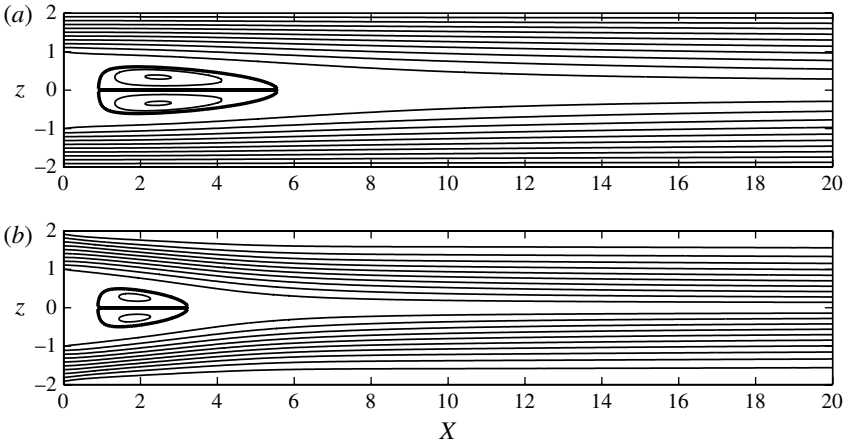

FIGURE 1. Streamlines of two of the confined wake flows studied in this paper. Both flows have inverse shear ratio $\Lambda^{-1} = -1.2$ and confinement parameter $h = 1$. (*a*) Free slip at the boundaries; (*b*) no slip at the boundaries.

instabilities that appear in paper manufacturing, (Lundell, Söderberg & Alfredsson 2011; Tammisola *et al.* 2011), and partly by instabilities that appear in rocket and aircraft engines (Juniper & Candel 2003).

The above flows tend to be at high Reynolds numbers, for which confinement increases global instability. This is seen particularly clearly in the experimental study of Richter & Naudascher (1976). They examined the fluctuating forces on a confined circular cylinder at $10^4 < Re < 10^6$ and found that the fluctuating cross-stream force, which arises from sinuous vortex shedding, increases markedly as the flow is confined. The same effect was observed in a numerical study by Kim, Yang & Senda (2004), and by Bearman & Zdravkovich (1978) and Hwang & Yao (1997) for the half-confined case. Confinement destabilizes wake flows at intermediate Reynolds numbers as well, as is seen, for example, in Davis, Moore & Purtell (1983) at $Re = 750$.

For the rotating-disk boundary layer, Healey (2007) showed that confinement has a singular effect on waves that both propagate and grow in the cross-stream direction. The presence of confining walls, however far away, sets up standing waves that can make a confined flow absolutely unstable even when the equivalent unconfined flow is convectively unstable. This analysis was later extended to jets and wakes by Juniper (2007). In the current study, however, there are no waves that both propagate and grow in the cross-stream direction in the equivalent unconfined flow, so the mechanism described in Healey (2007) is not active.

The effect of confinement is less well understood at low and moderate Reynolds numbers. In this paper, we examine viscous wake flows, such as those shown in figure 1, at $Re = 100$. Two incompressible flows with uniform viscosity are injected through the left boundary: a fast-moving outer flow and a slow-moving inner flow. When the inner flow is sufficiently slow-moving, a recirculation zone forms just downstream of the injection plane. The whole flow is confined between two flat plates. The ratio of the width of the outer flow to the half-width of the inner flow, which is labelled h, turns out to have a strong influence on the flow's stability.

Local stability analyses of jets and wakes with piecewise-linear velocity profiles, such as in Juniper (2006, 2007), show that inviscid flows become more absolutely unstable when confined. Co-flow inviscid planar jets are convectively unstable at all

h but they become marginally absolutely unstable to a varicose mode at $h = 2.79$. Co-flow inviscid planar wakes are convectively unstable at large h but they become absolutely unstable to a sinuous mode at $h = 2.79$ and reach maximum absolute instability at $h = 1$, when the outer flow has exactly half the width of the inner flow. This result is exploited in cryogenic rocket engines in order to enhance break-up of the slow-moving liquid oxygen stream by the fast-moving hydrogen stream; Juniper & Candel (2003).

Although the effect of confinement is clear for inviscid flows, our previous studies of viscous flows at $Re \sim 10^2$ seem to contradict each other. On the one hand, a local stability analysis of viscous planar wakes without boundary layers (Rees & Juniper 2010) shows that the destabilizing effect of confinement persists down to $Re = 10$, although it becomes attenuated at lower Reynolds numbers because the instability itself becomes attenuated by viscosity. This destabilizing effect, attenuated by viscosity, is also seen at $Re = 500$ and $Re = 100$ in the nonlinear direct numerical simulations (DNS) of Biancofiore, Gallaire & Pasquetti (2011). On the other hand, linear global stability analyses of confined viscous planar wakes with boundary layers (Tammisola *et al.* 2011) show that wakes at $Re = 100$ become more globally stable when confined. This is observed both for the linear global modes and in nonlinear DNS. At first sight, these results seem to contradict those of Rees & Juniper (2010) because stronger absolute instability should imply a stronger global instability. In this paper, we examine these confined flows in more detail in order to explain this apparent contradiction and to highlight the influence of the boundary layers, which was not considered in detail in Rees & Juniper (2010).

2. Methodology

We perform two types of analysis on two types of flow. The first type of flow has free slip at the confining walls; the second has no slip at the confining walls. In the second type of flow, the boundary layers affect the stability of the shear layers and also block the flow near the wall, which shortens the recirculation bubble by forcing the flow to speed up near the centreline. By considering both flows with both analyses, we can separate the effect of confinement from the two effects caused by the boundary layers.

The properties of each flow are characterized by the conditions on the left boundary, where the inner flow has velocity U_1^* and width h_1^* and the outer flow has velocity U_2^* and width h_2^* and $*$ denotes dimensional variables. The shear between the two flows is quantified by the inverse shear ratio $\Lambda^{-1} \equiv (U_1^* - U_2^*)/(U_1^* + U_2^*)$. The confinement is quantified by the ratio $h \equiv h_2^*/h_1^*$. (In Rees & Juniper 2010, it was quantified by $h_{RJ} \equiv (h_2^* - h_1^*)/(h_2^* + h_1^*) = (h - 1)/(h + 1)$.) The viscosity is quantified by the Reynolds number, which is defined as $Re \equiv U_2^* h_1^*/\nu^*$ where ν is the kinematic viscosity. (In Rees & Juniper 2010, it was quantified by $Re_{RJ} \equiv (U_1^* + U_2^*)(h_1^* + h_2^*)/(2\nu^*) = (1 + h)/(1 - \Lambda)Re$.) For each type of flow we vary Λ^{-1} at $h = 1$ in order to test the effect of Λ^{-1} and then we vary h at $\Lambda^{-1} = -1.2$ in order to test the effect of h.

Our first type of analysis is a linear global stability analysis (Tammisola *et al.* 2011). The Navier–Stokes equations are linearized about the steady but unstable base flow and small perturbations are assumed of the form $\tilde{\boldsymbol{u}}(x, z)\exp(-\mathrm{i}\omega_g t)$. The evolution operator for the perturbations is discretized and expressed as a matrix acting on the discretized state vector $\tilde{\boldsymbol{u}}(x, z)$. The global modes of the linearized system are the eigenmodes of this matrix. Each eigenmode consists of an eigenvalue, ω_g, which

describes the frequency and growth rate, and an eigenvector, $\tilde{\boldsymbol{u}}(x, z)$, which describes the mode shape. The procedure for finding the eigenmodes of this matrix is described in § 3.

Our second type of analysis is a linear local stability analysis (Huerre & Monkewitz 1990). As for the global analysis, the Navier–Stokes equations are linearized about the steady but unstable base flow. The WKBJ approximation is applied, i.e. the base flow is assumed to be locally parallel and small local perturbations are assumed of the form $\hat{\boldsymbol{u}}(z)\exp\{\mathrm{i}(kx - \omega t)\}$. The absolute frequency ω_0 is calculated at each slice and the frequency and growth rate of the linear global mode, ω_g, are estimated by analytical continuation into the complex x-plane. The response of each slice at ω_g is then calculated and the WKBJ approximation is inverted in order to obtain the mode shape $\tilde{\boldsymbol{u}}(x, z)$. This procedure is described in § 4.

3. The global analysis

3.1. *Construction of the global analysis*

The flow is assumed to be governed by the Navier–Stokes (N–S) equation and the incompressibility condition:

$$\frac{\partial \boldsymbol{U}_{tot}}{\partial t} + \boldsymbol{U}_{tot}\cdot\boldsymbol{\nabla}\boldsymbol{U}_{tot} = -\boldsymbol{\nabla}P_{tot} + \frac{1}{Re}\nabla^2\boldsymbol{U}_{tot}, \tag{3.1}$$

$$\boldsymbol{\nabla}\cdot\boldsymbol{U}_{tot} = 0. \tag{3.2}$$

Following our previous studies, the flow is assumed not to vary in the spanwise direction, y. The total velocity and pressure fields are divided into steady and time-varying components:

$$\boldsymbol{U}_{tot}(x, z, t) = \boldsymbol{U}(x, z) + \boldsymbol{u}(x, z, t), \tag{3.3}$$

$$P_{tot}(x, z, t) = P(x, z) + p(x, z, t). \tag{3.4}$$

The steady base flow $(\boldsymbol{U}(x, z), P(x, z))$ is the solution to the N–S equations (3.1)–(3.2) without time derivatives. The unsteady perturbation is assumed to take the form

$$\boldsymbol{u}(x, z, t) = \tilde{\boldsymbol{u}}(x, z)\exp\left(-\mathrm{i}\omega_g t\right). \tag{3.5}$$

The N–S equations are linearized around the base flow by ignoring quadratic terms in perturbation quantities, to give the linearized N–S equations (LN–S):

$$-U\partial_x\hat{u} - V\partial_z\hat{u} - \hat{u}\partial_x U - \hat{v}\partial_z U - \partial_x\hat{p} + \frac{1}{Re}\left(\partial_{xx}\hat{u} + \partial_{zz}\hat{u}\right) = -\mathrm{i}\omega_g\hat{u}, \tag{3.6}$$

$$-U\partial_x\hat{v} - V\partial_z\hat{v} - \hat{u}\partial_x V - \hat{v}\partial_z V - \partial_z\hat{p} + \frac{1}{Re}\left(\partial_{xx}\hat{v} + \partial_{zz}\hat{v}\right) = -\mathrm{i}\omega_g\hat{v}, \tag{3.7}$$

$$\partial_x\hat{u} + \partial_z\hat{v} = 0. \tag{3.8}$$

The LN–S equations (3.6)–(3.8) constitute a two-dimensional eigenvalue problem for ω_g. This set of equations is satisfied only for certain eigenvalues, ω_g, which give the growth rates and frequencies of the linear global modes. (We call ω_g the *complex frequency*.) Each ω_g has an associated eigenfunction $\tilde{\boldsymbol{u}}(x, z)$, which describes the shape of the global mode.

A finite number of the most unstable modes can approximate the dynamics of the flow, as described in Schmid (2007). In most of the cases presented in this paper, there is only one mode with positive growth rate, which dominates the dynamics after the initial transients have died away. In this paper, we focus only on this global mode.

3.2. *Solution of the global analysis*

The base flow is obtained from DNS using a Legendre polynomial-based spectral-element method (SEM) implemented in the code `nek5000` (Fischer 1997). The inlet velocity has a slightly smoothed top-hat profile with slower velocity in the inner flow:

$$U(0, z > 0) = \frac{1}{\pi}\left[\arctan(500(h + 1 - z)) + \frac{\pi}{2}\right] + \frac{2}{\pi(\Lambda^{-1} - 1)}\left[\arctan(500(1 - z)) + \frac{\pi}{2}\right]. \tag{3.9}$$

A symmetry condition is imposed along the centreline, $z = 0$. For these base flows, all the unstable modes are antisymmetric, which means that the DNS converges naturally to the steady (but antisymmetrically unstable) solution.

At the wall boundary ($z = h + 1$), we set either a no-slip condition or a free-slip condition (figure 1). At the downstream boundary, we set a homogeneous Neumann condition for the velocities and a homogeneous Dirichlet condition for the pressure. The possible influence of the downstream boundary condition is eliminated by using substantially longer domains for the base flow than are used in the stability problem. For more details about the code and base flow computations, see Tammisola *et al.* (2011).

To calculate the linear global modes, (3.6)–(3.8) are discretized in space using Chebyshev polynomials in both the streamwise and cross-stream directions:

$$\hat{u}(x, z) \approx \sum_{i=1}^{N_x}\sum_{j=1}^{N_z} c_{ij}\phi^i(x)\phi^j(z) \tag{3.10}$$

where ϕ^k is the kth Chebyshev polynomial. The values of the unknown coefficients c_{ij} are obtained by requiring the discretized equations to be satisfied exactly at the $N_x \times N_z$ collocation points. The domain is linearly transformed from $[-1, 1] \times [-1, 1]$ to $[0, L] \times [0, h_1 + h_2]$. For the calculations, $L = 80$ or 120, but only the upstream region is plotted in this paper. There are $N_x = 200$ gridpoints for $L = 120$ and the eigenvalues are independent of grid spacing to the fourth decimal place. The Chebyshev distribution of gridpoints is not optimal for this problem but was retained for convenience. Further details about the numerics and convergence can be found in Tammisola *et al.* (2011).

For all base flows, whether they have free slip or no slip at the confining walls, we set a no-slip condition for the perturbation:

$$\hat{u}(x, h + 1) = 0, \quad \hat{v}(x, h + 1) = 0. \tag{3.11}$$

For the wake flows in this paper, it is sufficient to consider only antisymmetric modes:

$$\hat{u}(x, 0) = 0, \quad \partial_z\hat{v}(x, 0) = 0, \quad \hat{p}(x, 0) = 0. \tag{3.12}$$

The truncation of the domain in the streamwise direction is problematic because the only natural streamwise boundary condition for unstable global modes is to decay at infinity. We impose a Dirichlet condition at the inlet and a Neumann condition at the outlet:

$$\hat{u}(0, z) = 0, \quad \hat{v}(0, z) = 0, \tag{3.13}$$

$$\partial_x\hat{u}(L, z) = 0, \quad \partial_x\hat{v}(L, z) = 0. \tag{3.14}$$

We check that these boundary conditions do not affect the stability by ensuring that the most unstable eigenvalue is not sensitive to the domain length and that the upstream influence of the Dirichlet condition is small (Tammisola *et al.* 2011).

Using these techniques, the eigenvalue problem of a continuous operator (3.6)–(3.8) with boundary conditions (3.13)–(3.14) is transformed into a generalized matrix eigenvalue problem:

$$\boldsymbol{A}\boldsymbol{q} = \omega_g \boldsymbol{B}\boldsymbol{q}, \tag{3.15}$$

where $\boldsymbol{q} = (\hat{u}, \hat{v}, \hat{p})$ is the eigenvector and ω_g the eigenvalue. The number of elements of the left-hand side matrix $\boldsymbol{A}$ grows as $9N_x^2N_z^2$ (compared to N_z^2 in the local analysis) and the required memory increases correspondingly. To handle this, the matrix is built in parallel and the eigenvalue problem solved using parallel versions of the Arnoldi algorithm, with linear algebra operations from ScaLAPACK (Tammisola *et al.* 2011).

4. The local analysis

4.1. *Construction of the local analysis*

As for the global analysis, the velocity and pressure fields are decomposed into a steady base flow, $(\boldsymbol{U}(x, z), P(x, z))$, and a small perturbation, $(\boldsymbol{u}(x, z, t), p(x, z, t))$. For the local analysis, however, we assume that the flow exhibits two well-separated length scales: an instability wavelength, λ, and a length scale that characterizes the streamwise non-uniformity of the base flow, L. The ratio λ/L, which must be small for a local analysis to be rigorously valid, is labelled ϵ.

The development in this paper follows Monkewitz, Huerre & Chomaz (1993), which is summarized pedagogically in Huerre & Monkewitz (2000, § 4). The LN–S equations for the small perturbation contain terms that scale with ϵ^0, terms that scale with ϵ^1 and terms, which are neglected, that scale with higher orders of ϵ. The ϵ^0 terms represent a streamwise succession of locally parallel problems, which are solved with the technique described in § 4.2. The complex frequency, ω_g, of the linear global mode and the position of the wavemaker region, X_s, are calculated with the technique described in § 4.3. The corresponding global mode shape is calculated in § 4.4 by integrating

$$\boldsymbol{u}(x, z, t) \sim A_0(X)\hat{\boldsymbol{u}}^{\pm}(z; X) \exp\left(\frac{\mathrm{i}}{\epsilon}\int_0^X k^{\pm}(X'; \omega)\,\mathrm{d}X' - \omega_g t\right), \tag{4.1}$$

where, at the X-position of each slice, k^+ is the local wavenumber downstream of X_s, k^- is the local wavenumber upstream of X_s, and $\hat{\boldsymbol{u}}^{\pm}(z; X)$ is the corresponding eigenfunction. The ϵ^1 terms of the LN–S equations describe the evolution of the slowly varying amplitude $A_0(X)$. In this paper, we assume that A_0 is uniform. In § 5.1, we conclude that the influence of this assumption is much smaller than the influence of the inaccuracies in $k^{\pm}$.

4.2. *Solution of the locally parallel problem*

The planar LN–S equations for the perturbation are expressed as three PDEs in three primitive variables, (u, v, p). At each X-position, the perturbations are expressed as Fourier modes such as $u(x, z, t) = \hat{u}(z)\exp\{\mathrm{i}(kx - \omega t)\}$, which converts the three PDEs into three ODEs. The ODEs are discretized on a Chebyshev-spaced grid in the z-direction, which produces a generalized matrix eigenvalue problem of the form

$$\boldsymbol{A}(k)\boldsymbol{\phi} = \omega \boldsymbol{B}(k)\boldsymbol{\phi} \tag{4.2}$$

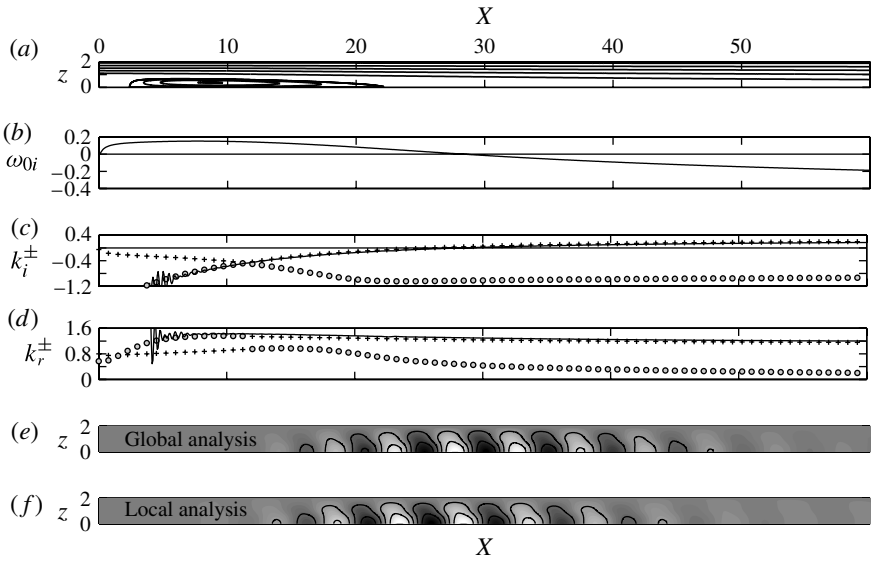

FIGURE 2. The base flow (*a*), local stability properties (*b–d*) and global modes (*e*,*f*) of a confined planar wake with $h = 1$, $\Lambda^{-1} = -1.2$, $Re = 400$ and free-slip boundaries. (*a*) Streamlines; (*b*) absolute growth rate, ω_{0i}; (*c*) spatial growth rates, k_i^+ (+) and k_i^- (○), calculated with the local analysis, compared with k_i (—) extracted from the global analysis (the latter is noisy at the upstream end because the amplitude is small); (*d*) as for (*c*) but for the real spatial wavenumbers, $k_r^{\pm}$; (*e*) $\tilde{v}(x, z)$ of the first eigenmode calculated with the global analysis; (*f*) $\tilde{v}(x, z)$ of the first eigenmode calculated with the local analysis. For these calculations, the streamwise length equals 120, but only the upstream region is shown.

where $\boldsymbol{\phi}$ is a column vector representing the discretized values of $\hat{u}$, $\hat{v}$ and $\hat{p}$. This is satisfied for certain (ω, k) pairs and represents the dispersion relation for this slice of the flow. In this paper, 108 Chebyshev-spaced points are used between the centreline and top wall, which is sufficient that the eigenvalues change by $\sim 10^{-5}$ when the resolution is increased.

A temporal stability analysis is performed on a slice near the entry plane to find the maximum temporal growth rate, which corresponds to the growth rate of the centre of the impulse response in a parallel flow (Juniper 2007). A spatio-temporal stability analysis is then performed by finding the saddle points of $\omega(k)$ that are also k^+/k^- pinch points. (In a flow with mean mass flux in the positive x-direction, the perturbation with maximum temporal growth rate lies on the k^+ branch and the algorithm used in this paper finds all the k^- branches that pinch with it.) In wake flows such as those studied here, there can be up to three such k^+/k^- saddles (Juniper 2006). The highest saddle is labelled the *dominant* saddle point. These saddle points are then followed as the base flow changes. The absolute complex frequency of the dominant saddle, ω_0, as a function of streamwise distance, X, is stored for the algorithm in § 4.3. An example of $\omega_{0i}(X)$ is shown in figure 2(*b*).

4.3. *Calculating the frequency and growth rate of the linear global mode*

It is assumed that the absolute complex frequency $\omega_0(X)$ can be continued analytically into the complex X-plane. The complex frequency of the linear global mode, ω_g, is given at leading order in ϵ by the saddle point of $\omega_0(X)$, which is labelled $\omega_s(X_s)$ (Chomaz, Huerre & Redekopp 1991). In this paper, the position of the saddle point

X_s is estimated by selecting the region of $\omega_0(X)$ around the maximum of $\omega_{0i}(X)$ and then fitting Padé polynomials to these values. (Padé polynomials take the form $P^n(x)/Q^m(x)$, where $P^n(x)$ and $Q^m(x)$ are polynomials of order n and m respectively.) Padé polynomials have two advantages over standard polynomials: they can fit $\omega_0(X)$ accurately at relatively low order, and they are better behaved in the complex plane (Cooper & Crighton 2000).

Initially, the saddle position, X_s, is found for $n = m = 2$ by considering a small region around the maximum of $\omega_{0i}(X)$. The saddle is then followed as n and m are increased to 8 and the threshold value of ω_{0i} is lowered until the polynomials fit a wide range of $\omega_0(X)$ around the absolutely unstable region. This gives the complex frequency ω_g of the global mode and the position of the wavemaker region X_s. If n and m are increased further, there is no systematic change in the saddle position but its variance around the value at $n = m = 8$ increases. From this, we conclude that, for larger n and m, the saddle position becomes unduly influenced by small errors in $\omega_0(X)$, without becoming more accurate.

These results can be compared with those from other local analyses. For the steady but unstable flow behind a cylinder at $Re = 50$, Pier (2002) found the real part of ω_g to be 0.78, while Giannetti & Luchini (2007) found $\omega_g = 0.779 + 0.09\mathrm{i}$. The process used in this study finds $\omega_g = 0.789 + 0.0918\mathrm{i}$ for the same flow. Given that the calculated value of ω_g varies slightly with n and m and with the streamwise extent of $\omega_0(X)$ that is sampled, this is sufficiently close for us to have confidence in the procedure.

These results can also be compared with those from global analyses (§ 3). Giannetti & Luchini (2007) compared a linear global analysis with a linear local analysis of the flow behind a cylinder at $15 < Re < 100$ and showed that the local analysis always over-predicts ω_{gi}. At $Re = 50$, their global analysis predicts $\omega_g = 0.747 + 0.0125\mathrm{i}$, showing that their local analysis over-predicts ω_{gi} by 0.08. At $Re = 100$, which is the value used for most of the results in this paper, their local analysis over-predicts ω_{gi} by 0.059. Given that the flows in this paper are very similar to the flow behind a cylinder, we expect a similar over-prediction in this paper.

4.4. *Calculating the two-dimensional global mode shape*

The two-dimensional global mode shape is calculated by investigating how the flow responds to an oscillation with complex frequency ω_g, so that the integral (4.1) can be evaluated. To do this, the values of k that satisfy (4.2) when $\omega = \omega_g$ are calculated and the two that correspond to the k^+ and k^- branches in the X-plane are selected. The global mode is estimated from (4.1) by integrating the k^- branch upstream of X_s and the k^+ branch downstream of X_s. The z-dependence is obtained by multiplying the result by the eigenfunction of the k^- branch upstream of X_s and that of the k^+ branch downstream of X_s.

5. Comparison of local and global results

In this section, results from the global analysis are compared with those of the local analysis for two wake flows: one at $Re = 400$ and the other at $Re = 100$.

5.1. $Re = 400$

Figure 2 shows local and global results for a confined wake flow at $Re = 400$ with $h = 1$, $\Lambda^{-1} = -1.2$ and a free-slip condition at the walls. There is a recirculation zone between $2.36 < X < 22.29$. Taking the distance to the end of this recirculation zone as a characteristic streamwise evolution length scale, L_e, we obtain $L_e \approx 20$.

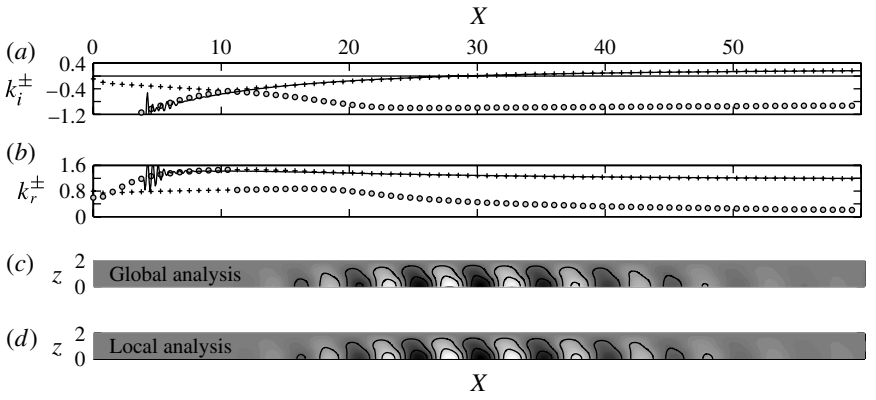

FIGURE 3. As for figure 2(*c–f*) but with $k^{\pm}$ calculated at the complex frequency of the global analysis, $\omega_g(\text{glob})$, rather than that of the local analysis, $\omega_g(\text{loc})$.

The absolutely unstable region lies between $0.06 < X < 28.42$. Continuing ω_0 analytically into the complex X-plane, the complex global frequency is found to be $\omega_g(\text{loc}) = 0.6547 + 0.1306\text{i}$. The k^+ and k^- branches are calculated at $\omega_g(\text{loc})$ and are plotted in figure 2(*c*,*d*) alongside the complex local wavenumber, k, extracted from the global analysis. This is extracted by assuming that $\tilde{\boldsymbol{u}}(x, z)$ in (3.5) is locally of the form $\hat{\boldsymbol{u}}(z)\exp(\text{i}kx)$ such that $k = (-\text{i}/\hat{\boldsymbol{u}})\,\mathrm{d}\hat{\boldsymbol{u}}/\mathrm{d}x$. This is calculated from the v-velocity eigenfunction at $z = 0$ with no further treatment. The complex local wavenumber, k, closely follows the k^- branch upstream of the wavemaker region and the k^+ branch downstream, as expected.

The global analysis gives a complex global frequency of $\omega_g(\text{glob}) = 0.6659 + 0.1133\text{i}$, which is slightly more stable than that of the local analysis, as expected from § 4.3. (Being at $Re = 400$, the flow is more locally parallel and the difference is therefore smaller than at $Re = 100$.) The global analysis gives the two-dimensional eigenfunction in figure 2(*e*), while, by integrating (4.1), the local analysis gives the two-dimensional eigenfunction in figure 2(*f*), which is very similar. The slightly higher growth rate in the local analysis causes the centre of its global mode to be slightly further upstream. This is a general feature of the global mode predicted by the local analysis. Having calculated the $k^{\pm}$ branches and the mode shapes, we can estimate that $\lambda \approx 5.0$, which means that $\epsilon \approx 0.25$. The local analysis works well at this value of ϵ.

Figure 3 shows the k^+ and k^- branches and the two-dimensional eigenfunctions calculated using the local analysis, but at the complex frequency calculated by the global analysis, $\omega_g(\text{glob})$. Frames (*c*) and (*d*) are almost identical, which shows that it is accurate to assume that $A(X)$ is uniform and that the only significant defect of the local analysis is its over-prediction of ω_{gi} and the consequent error in $k^{\pm}$.

In summary, the global analysis gives the more accurate prediction of the absolute frequency and the two-dimensional eigenfunctions because it does not make the parallel flow assumption. However, the local analysis gives the more useful qualitative information about the flow. For instance it shows that, although the global mode has a maximum amplitude at $X = 28.36$, it is actually driven by a wavemaker region at $X = 12.43$, which arises from the absolutely unstable region between $0.06 < X < 28.42$, which is centred on the recirculation zone. The flow downstream of the recirculation zone is simply responding to the forcing from this region.

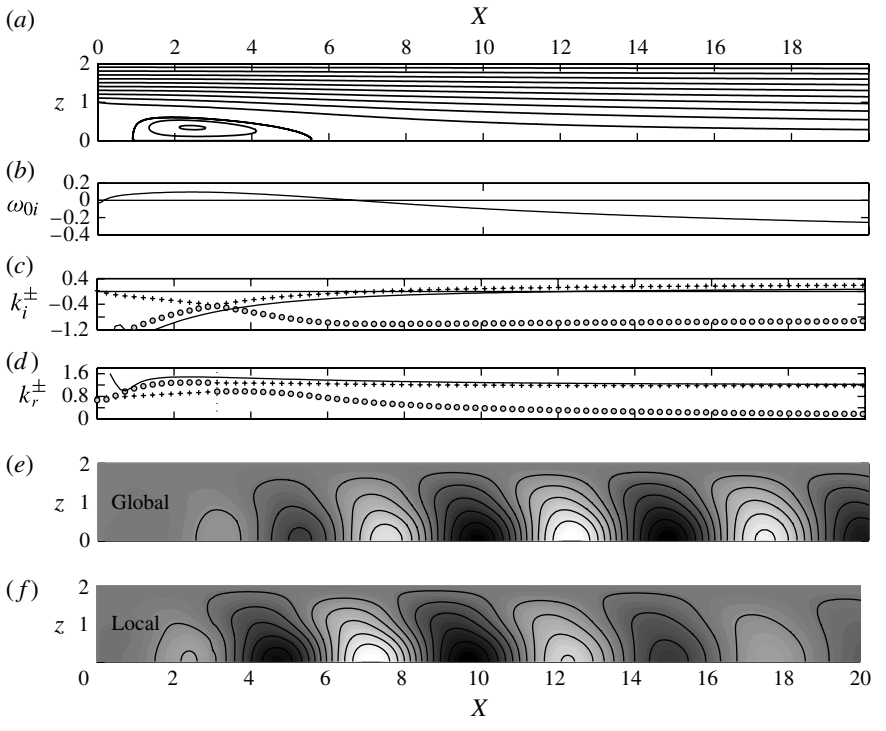

FIGURE 4. As for figure 2, but for $Re = 100$.

5.2. $Re = 100$

Figure 4 shows results for a confined wake flow at $Re = 100$ with $h = 1$, $\Lambda^{-1} = -1.2$ and a free-slip condition at the walls. There is a recirculation zone between $0.91 < X < 5.57$. Taking the distance to the end of this recirculation zone as a characteristic streamwise evolution length scale, L_e, we obtain $L_e \approx 6$. The absolutely unstable region lies between $0.17 < X < 6.69$. From this, the complex global frequency is found to be $\omega_g(\text{loc}) = 0.6538 + 0.08594\text{i}$. The k^+ and k^- branches are calculated at $\omega_g(\text{loc})$ and are plotted in figure 4(*c*,*d*) alongside the complex local wavenumber, k, extracted from the global analysis. The complex local wavenumber, k, follows the k^- branch upstream of the wavemaker region and the k^+ branch downstream, but is not as close as it was in the $Re = 400$ case.

The global analysis gives a complex global frequency of $\omega_g(\text{glob}) = 0.6613 + 0.02665\text{i}$, which is 0.059 more stable than that of the local analysis, as expected from § 4.3. The global analysis gives the two-dimensional eigenfunctions in figure 4(*e*), while the local analysis gives the two-dimensional eigenfunctions in figure 4(*f*). The agreement is reasonable but not excellent. Again, the higher growth rate in the local analysis causes the centre of its global mode to be slightly further upstream. Having calculated the $k^{\pm}$ branches and the mode shapes, we can estimate that $\lambda \approx 5.1$, which means that $\epsilon \approx 0.8$. This is too large to expect the WKBJ analysis to be accurate.

Figure 5 shows the k^+ and k^- branches and the two-dimensional eigenfunctions calculated with the local analysis, but at the complex frequency calculated with the global analysis, $\omega_g(\text{glob})$. This gives a more accurate prediction of the two-dimensional eigenfunction than was obtained with $\omega_g(\text{loc})$. This shows that, for this

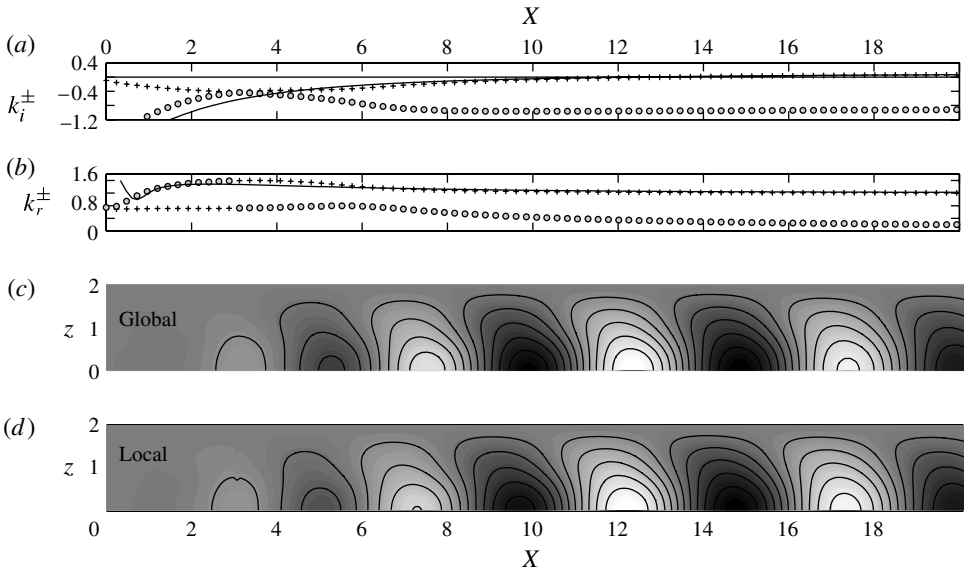

FIGURE 5. As for figure 3, but for $Re = 100$.

flow, the inaccuracy in the local analysis lies in the prediction of ω_g, rather than in the calculation of the $k^{\pm}$ branches downstream. This is because the local analysis is less accurate in the upstream regions, which determine ω_g, because the flow is locally non-parallel there. By contrast, the local analysis is accurate in the downstream regions because the flow is nearly locally parallel there.

Given that the inaccuracy of the local analysis lies in the prediction of ω_g, it is reasonable to ask whether adding $O(\epsilon)$ corrections would be beneficial, as in (6.1) of Monkewitz *et al.* (1993). We do not attempt to answer that question because the calculations are tortuous and may not be conclusive without considering $O(\epsilon^2)$ and $O(\epsilon^3)$ corrections as well, which would be unfeasible. Nevertheless, our results show that the inaccuracy in the prediction of ω_g increases as ϵ increases, which is consistent with the idea that adding higher-order corrections would be beneficial. In detail: for the $Re = 400$ case, $\epsilon \approx 0.25$ and the inaccuracy in ω_g, defined as $abs\{\omega_g(\text{loc}) - \omega_g(\text{glob})\}$, is 0.021; for the $Re = 100$ free-slip case, $\epsilon \approx 0.8$ and the inaccuracy in ω_g is 0.059; and for the $Re = 100$ no-slip case (table 1, $\Lambda^{-1} = -1.20$), $\epsilon \approx 1.5$ and the inaccuracy in ω_g is 0.160.

6. Effect of shear ratio

The growth rate and frequency of the linear global mode are plotted in figure 6 and table 1 for flows with $Re = 100$, $h = 1$ and varying Λ^{-1}. The top frames show flows with free slip at the boundaries. The bottom frames show flows with no slip at the boundaries. As the co-flow increases (as Λ^{-1} becomes more negative), the global modes become more stable and oscillate at higher frequencies. We will use the local analysis to find the physical origin of these trends.

There is a nearly systematic offset between the complex frequencies calculated with the local analysis and those calculated with the global analysis, very similar to that found by Giannetti & Luchini (2007). The real part of this offset is smaller for the free-slip case, for which $\epsilon \approx 0.8$, than it is for the no-slip case, for which $\epsilon \approx 1.5$,

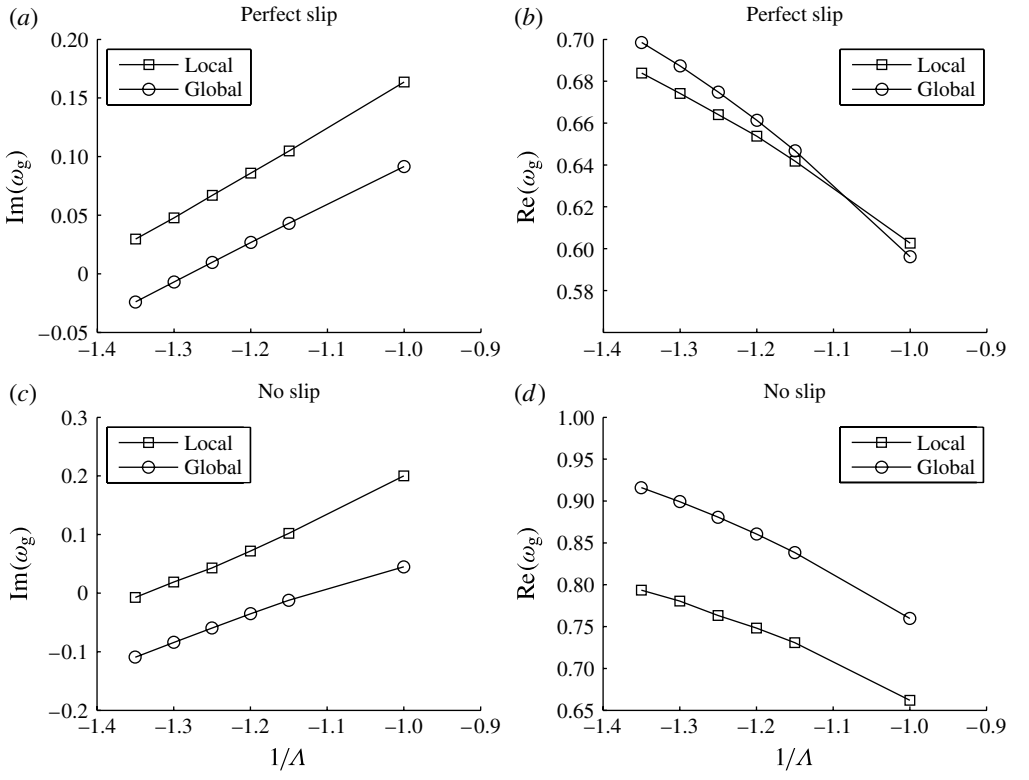

FIGURE 6. Growth rate, ω_{gi} (*a*,*c*) and frequency, ω_{gr} (*b*,*d*) of the linear global mode calculated with the local analysis (squares) and the global analysis (circles) for free-slip boundaries (*a*,*b*) and no-slip boundaries (*c*,*d*).

because the free-slip case is closer to being locally parallel. The imaginary part of this offset is always around 0.059.

The streamlines, the absolutely unstable regions (light grey), and the wavemaker region (dark grey) are shown in figure 7(*a*) for the case with free slip and in figure 8(*a*) for the case with no slip. The local absolute growth rate, ω_{0i}, and the local k_i^+ and k_i^- branches are shown in figures 7(*b*) and 8(*b*).

For low co-flow (bottom frames) the region of absolute instability creates a globally unstable flow, whose wavemaker region lies just downstream of the centre of the recirculating zone. As the co-flow increases (i.e. as Λ^{-1} becomes more negative), the recirculating zone becomes smaller and the flow becomes more stable.

The cases with no slip have smaller recirculation zones than the corresponding cases with free slip. This is the first reason why the cases with no slip are more globally stable than the cases with free slip, but it is not the only reason.

In the case with free slip, the absolutely unstable region extends into the co-flow region on both sides of the recirculation zone, similar to the results of Pier (2002) for an unconfined flow behind a cylinder. In the case with no slip, however, the absolutely unstable region does not extend into the co-flow region downstream of the recirculation zone. We can conclude that the second reason that the cases with no slip are more globally stable than the cases with free slip is that the proximity of the boundary layer to the shear layer makes the shear layer less locally unstable.

	Perfect slip		No slip	
Λ^{-1}	ω_g(loc)	ω_g(glob)	ω_g(loc)	ω_g(glob)
-1.00	$0.6026 + 0.163657\mathrm{i}$	$0.5961 + 0.091515\mathrm{i}$	$0.6621 + 0.200105\mathrm{i}$	$0.7597 + 0.044896\mathrm{i}$
-1.15	$0.6418 + 0.104847\mathrm{i}$	$0.6468 + 0.043247\mathrm{i}$	$0.7307 + 0.101872\mathrm{i}$	$0.8385 - 0.012174\mathrm{i}$
-1.20	$0.6538 + 0.085942\mathrm{i}$	$0.6613 + 0.026651\mathrm{i}$	$0.7482 + 0.071893\mathrm{i}$	$0.8606 - 0.035369\mathrm{i}$
-1.25	$0.6641 + 0.066963\mathrm{i}$	$0.6748 + 0.009889\mathrm{i}$	$0.7632 + 0.042795\mathrm{i}$	$0.8807 - 0.059537\mathrm{i}$
-1.30	$0.6742 + 0.047717\mathrm{i}$	$0.6873 - 0.006971\mathrm{i}$	$0.7805 + 0.018816\mathrm{i}$	$0.8992 - 0.084329\mathrm{i}$
-1.35	$0.6839 + 0.029651\mathrm{i}$	$0.6985 - 0.023865\mathrm{i}$	$0.7936 - 0.007261\mathrm{i}$	$0.9159 - 0.109491\mathrm{i}$

TABLE 1. Data in figure 6.

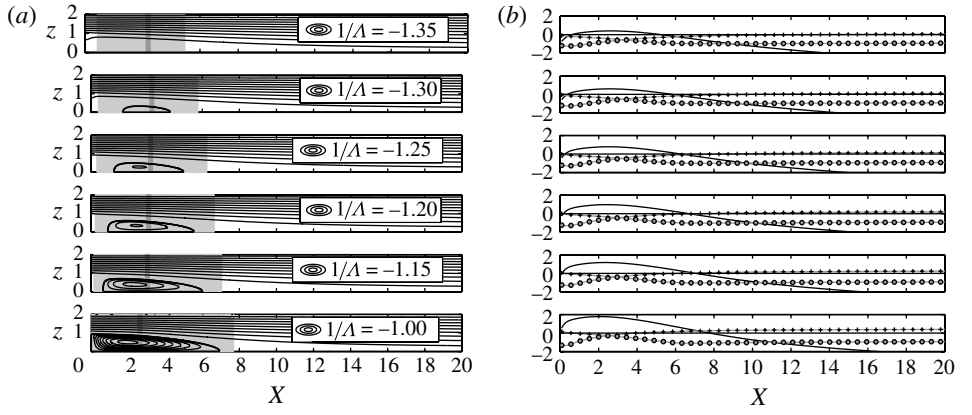

FIGURE 7. Streamlines (*a*) and ω_{0i} (—), k^+ (+) and k^- (∘) (*b*) for the free-slip case at $h = 1$ as Λ^{-1} varies. In (*a*) the absolutely unstable region is shown in light grey. The position of the wavemaker region is shown in dark grey. As the co-flow decreases (top to bottom), the recirculation zone strengthens and the flow becomes more absolutely unstable.

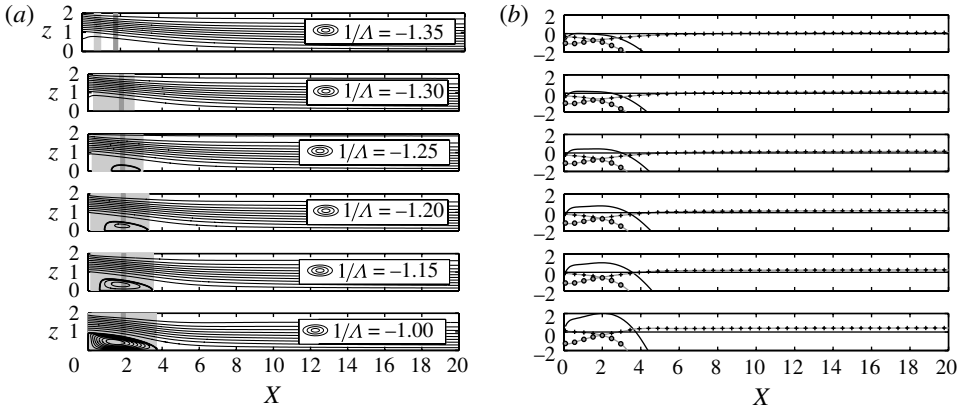

FIGURE 8. As for figure 7 but for the no-slip case. The same effect is seen at the upstream end of the recirculation bubble but the flow quickly becomes convectively unstable at the downstream end due to the boundary layers.

The eigenfunctions from the local analysis are compared with those from the global analysis in figure 9 (free slip) and 10 (no slip). They have the same qualitative structure and behaviour but there are some quantitative differences. When compared with the corresponding eigenfunction of the global analysis, each eigenfunction of the local analysis always has a slightly longer wavelength, more rapid growth at the upstream end, more rapid decay at the downstream end, and a centre that is further upstream. This is because each eigenfunction from the local analysis has a lower $k_r(X)$ and a higher $k_i(X)$ than the corresponding eigenfunction from the global analysis. This is exactly the trend seen in figure 4, and, when figure 4 is compared with figure 5, it is seen that this arises because the local analysis over-predicts the global growth rate (see figure 6). When the local analysis is repeated using the complex frequency derived from the global analysis, as in figure 5, the eigenfunctions from the local analysis are almost identical to those from the global analysis. As already mentioned,

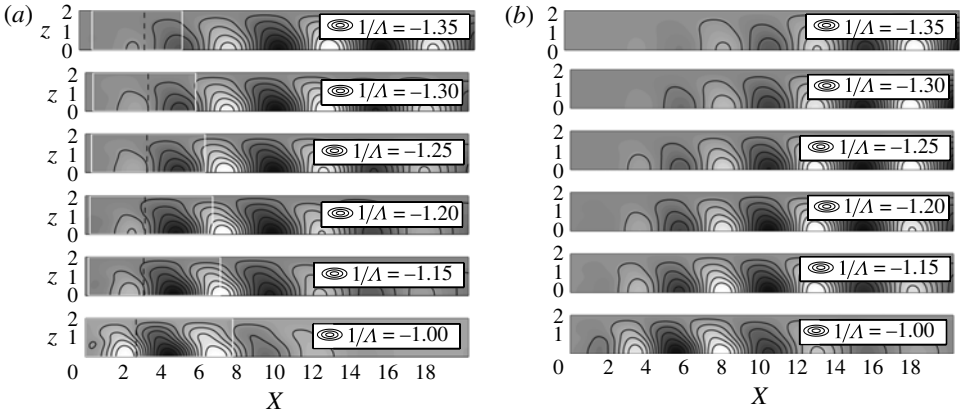

FIGURE 9. $\tilde{v}(x, z)$ eigenfunctions for the free-slip cases with $h = 1$ calculated with a local analysis (a) and a global analysis (b). The global mode lies further upstream for the local analysis because of its higher growth rate. For these calculations, the streamwise length, L, equals 120 but only the upstream region is shown.

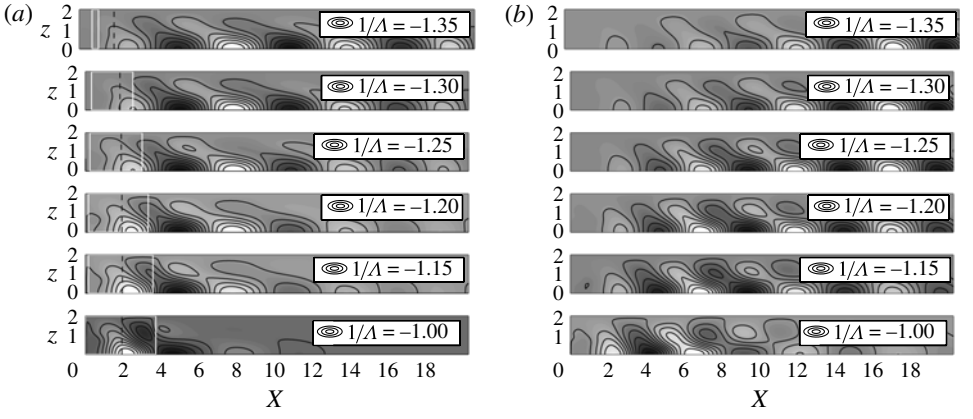

FIGURE 10. As for figure 9 but for the no-slip cases.

this over-prediction is a common feature of wake flows at this Reynolds number ($Re \sim 100$) (Giannetti & Luchini 2007). This defect of the local analysis arises because the flow is locally non-parallel. The local analysis becomes more accurate as the Reynolds number increases because the flow becomes more locally parallel.

7. Effect of confinement

The growth rate and frequency of the linear global mode are plotted as a function of h in figure 11 and table 2 for flows with $\Lambda^{-1} = -1.2$ and $Re = 100$ with free slip and no slip at the boundaries. For the free-slip cases, the flow is most unstable when $h \approx 1.5$. For the no-slip cases, the flow is barely affected by confinement when $h > 2$ but is strongly stabilized when $h < 2$. We will use the local analysis to find the physical origin of these trends.

The streamlines, the absolutely unstable regions, and the position of the wavemaker region are shown in figure 12(a) for the case with free slip and in figure 13(a) for the

	Perfect slip		No slip	
h	ω_g(loc)	ω_g(glob)	ω_g(loc)	ω_g(glob)
1.000	$0.6538 + 0.085942\mathrm{i}$	$0.6613 + 0.026651\mathrm{i}$	$0.7482 + 0.071893\mathrm{i}$	$0.8606 - 0.035369\mathrm{i}$
1.220	$0.6383 + 0.104380\mathrm{i}$	$0.6562 + 0.041594\mathrm{i}$	$0.7286 + 0.087469\mathrm{i}$	$0.8426 - 0.013077\mathrm{i}$
1.350	$0.6318 + 0.111333\mathrm{i}$	$0.6537 + 0.045078\mathrm{i}$	$0.7155 + 0.092530\mathrm{i}$	$0.8311 - 0.003578\mathrm{i}$
1.500	$0.6242 + 0.112461\mathrm{i}$	$0.6523 + 0.046319\mathrm{i}$	$0.7017 + 0.093950\mathrm{i}$	$0.8183 + 0.004457\mathrm{i}$
1.670	$0.6189 + 0.110243\mathrm{i}$	$0.6523 + 0.045606\mathrm{i}$	$0.6907 + 0.091285\mathrm{i}$	$0.8049 + 0.010542\mathrm{i}$
1.860	$0.6163 + 0.107583\mathrm{i}$	$0.6541 + 0.043574\mathrm{i}$	$0.6847 + 0.091329\mathrm{i}$	$0.7918 + 0.014624\mathrm{i}$
2.330	$0.6192 + 0.102644\mathrm{i}$	$0.6624 + 0.037869\mathrm{i}$	$0.6692 + 0.093271\mathrm{i}$	$0.7678 + 0.017788\mathrm{i}$
4.000	$0.6311 + 0.099269\mathrm{i}$	$0.6874 + 0.028373\mathrm{i}$	$0.6520 + 0.094551\mathrm{i}$	$0.7350 + 0.016713\mathrm{i}$
9.000	$0.6367 + 0.096425\mathrm{i}$	$0.7030 + 0.024166\mathrm{i}$	$0.6400 + 0.096620\mathrm{i}$	$0.7143 + 0.021059\mathrm{i}$
10.000	$0.6370 + 0.096776\mathrm{i}$	$0.7036 + 0.023956\mathrm{i}$	$0.6395 + 0.096926\mathrm{i}$	$0.7129 + 0.021374\mathrm{i}$

TABLE 2. Data in figure 11.

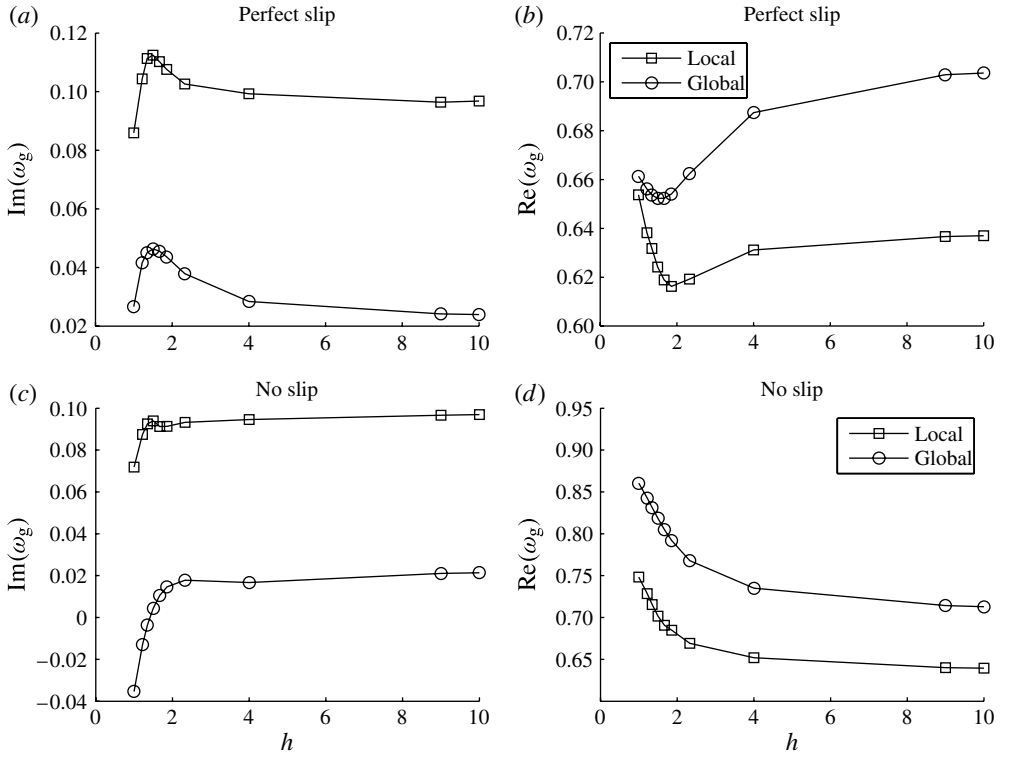

FIGURE 11. Growth rate, ω_{gi} (a,c) and frequency, ω_{gr} (b,d) of the linear global mode calculated with the local analysis (squares) and the global analysis (circles) for free-slip boundaries (a,b) and no-slip boundaries (c,d).

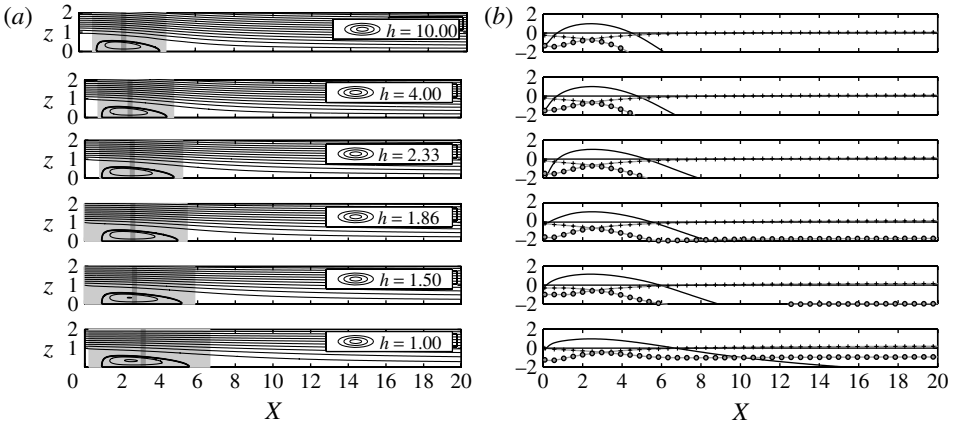

FIGURE 12. Streamlines (a) and ω_{0i} (—), k^+ (+) and k^- (○) (b) for the free-slip case at $\Lambda^{-1} = -1.2$ as h varies. The absolutely unstable region is shaded in light grey and the position of the wavemaker region is shown in dark grey.

case with no slip. The local absolute growth rate, ω_{0i}, and the k_i^+ and k_i^- branches are shown in figures 12(b) and 13(b).

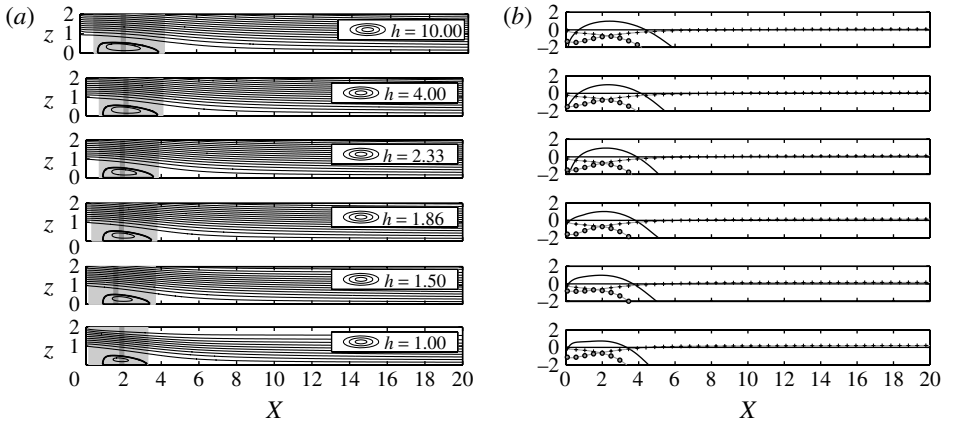

FIGURE 13. As for figure 12 but for the no-slip case.

When the confining walls are far away ($h \gg 1$), the recirculation zone of the case with free slip is almost the same size as that for the case with no slip and, as would be expected, the flows are equally unstable. As the flows become more confined, the recirculation zone of the case with free slip lengthens, while that of the case with no slip shortens. This is the first reason why the cases with free slip are more globally unstable than those with no slip. It is identical to the first reason in § 6. If this first effect acted alone, confinement would destabilize flows with free slip but stabilize flows with no slip.

When the confining walls become closer (h decreasing), the absolutely unstable region extends further downstream of the recirculation zone in the case with free slip but not in the case with no slip. This shows that the boundary layer velocity profile makes the shear layer less locally unstable, as seen in § 6. If this second effect acted alone, confinement would slightly destabilize flows with free slip but stabilize flows with no slip.

When the confining walls are close ($h < 2$), the absolutely unstable region upstream of the recirculation zone extends far into the co-flow region. This is the effect of confinement described by Rees & Juniper (2010). (In that paper, h is defined differently, such that h in this paper equals $(1 + h)/(1 - h)$ in that paper.) The global instability reaches a maximum (figure 11) around $h = 1.5$, which matches exactly the value of $h = 0.2$ at which Rees & Juniper (their figure 8*d*) predict that the absolute instability is maximal. If this third effect acted alone, confinement would destabilize flows with free slip (until $h \approx 1.5$) and also destabilize flows with no slip, probably to a similar value of h.

Through the local analysis, we can now explain the effect of confinement on the stability of viscous wake flows and explain the results in figure 11, which is the main aim of this paper. In the case with free slip, the three effects described above work together: confinement increases the size of the recirculation zone, extends the absolutely unstable region downstream of the recirculation zone and also extends it upstream of the recirculation zone, until $h \approx 1.5$. This explains the increased instability at $h \approx 1.5$ seen in figure 11(*a*). In the case with no slip, the first two effects work against the third: confinement decreases the size of the recirculation zone, slightly reduces the absolutely unstable region downstream of the recirculation zone but also extends it upstream of the recirculation zone, probably also until $h \approx 1.5$. At the

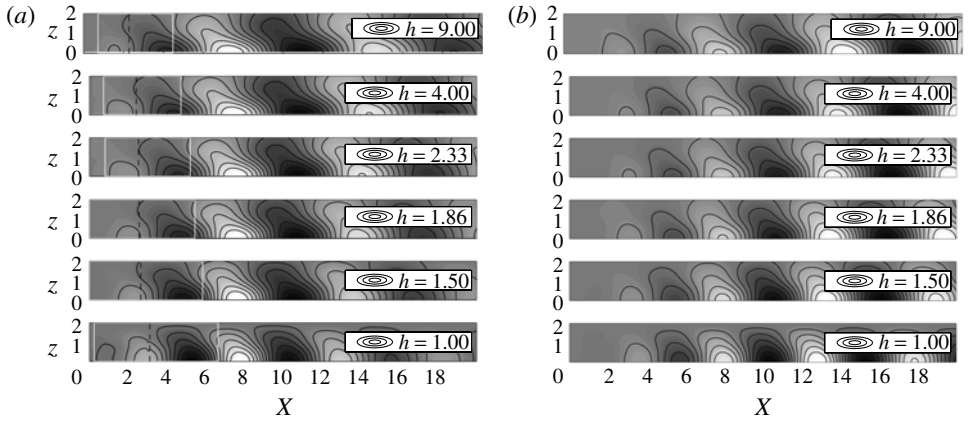

FIGURE 14. $\tilde{v}(x, y)$ eigenfunctions for the free-slip cases at $\Lambda^{-1} = -1.2$ calculated with a local analysis (*a*) and a global analysis (*b*). For these calculations, the streamwise length, L, equals 120 but only the upstream region is shown.

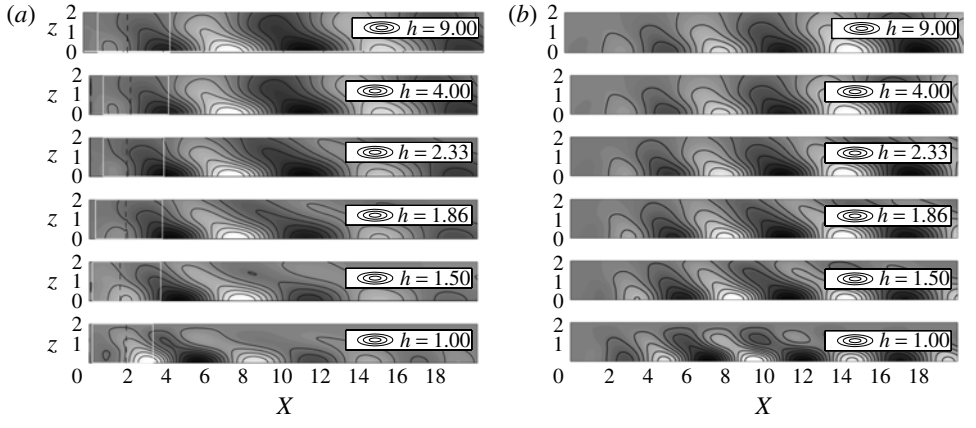

FIGURE 15. As for figure 14 but for the no-slip cases.

Reynolds number studied here, these effects almost exactly cancel out until $h \approx 1.5$, at which point all effects become stabilizing. In the local analysis of the no-slip case, there is a slight peak around $h = 1.5$ but this is not seen in the global analysis.

The eigenfunctions from the local analysis are compared with those from the global analysis in figures 14 (free slip) and 15 (no slip). The behaviour is the same as that seen in figures 9 and 10 and the difference arises because the flow is locally non-parallel. This is most noticeable in the no-slip cases at smaller values of h because the flow is more non-parallel for these flows than it is at larger values of h.

8. Conclusions

Confined wake flows are frequently found in industry and in model problems. Our previous work at high Reynolds numbers shows that confinement is destabilizing. Our previous work at medium to low Reynolds numbers, however, seems to give contradictory results. The aim of this paper is to resolve the apparent contradiction.

We consider, at $Re = 100$, two types of confined wake flows: one with free slip at the walls and one with no slip. We perform two types of analysis: a local stability analysis and a global stability analysis. These show that the global instability is caused by an absolutely unstable region centred on the recirculation zone. The local analysis always slightly over-predicts the global growth rate, as expected from previous work, but provides useful qualitative information about the effect of confinement on the flow.

We find that confinement acts in three ways: (i) it modifies the length of the recirculation zone, (ii) it brings the boundary layers closer to the shear layers, which changes their stability and (iii) it makes the flow more locally absolutely unstable when the confinement ratio, h, is around 1.5. Depending on the flow parameters, these effects can work with or against each other to destabilize or stabilize the flow.

In a flow with free slip, in which effect (ii) does not play a role, confinement lengthens the recirculation zone and also makes the flow more absolutely unstable around $h = 1.5$, both of which are destabilizing effects. Effects (i) and (iii) therefore work with each other to make the flow most globally unstable around $h = 1.5$, as seen in figure 11(*a*).

In a flow with no slip, confinement shortens the recirculation zone and brings the boundary layers closer to the shear layers, both of which are stabilizing. For $h > 1.5$, effects (i) and (ii) work against effect (iii) and confinement has little overall effect on the stability. For $h < 1.5$, effects (i) and (ii) work with effect (iii) and confinement has a strongly stabilizing effect. This can be seen in figure 11(*c*).

Rees & Juniper (2010) used a local analysis analysis to consider the third effect in isolation, while Tammisola *et al.* (2011) used a global analysis to consider all three effects together. These studies had contradictory results. By combining local and global analyses, we have been able to isolate the three effects described above and therefore resolve the apparent contradiction in our previous work. This shows the value of a combined local and global approach to shear flow instabilities, in which a global analysis gives accurate results, while a local analysis gives physical insight.

REFERENCES

BEARMAN, P. W. & ZDRAVKOVICH, M. 1978 Flow around a circular cylinder near a plane boundary. *J. Fluid Mech.* **89**, 33–47.

BIANCOFIORE, L., GALLAIRE, F. & PASQUETTI, R. 2011 Influence of confinement on a two-dimensional wake. *J. Fluid Mech.* (submitted).

CHOMAZ, J.-M., HUERRE, P. & REDEKOPP, L. 1991 A frequency selection criterion in spatially-developing flows. *Stud. Appl. Maths* **84**, 119–144.

COOPER, A. J. & CRIGHTON, D. G. 2000 Global modes and superdirective acoustic radiation in low-speed axisymmetrics jets. *Eur. J. Mech.* B **19**, 559–574.

DAVIS, R. W., MOORE, E. F & PURTELL, L. P. 1983 A numerical-experimental study of confined flow around rectangular cylinders. *Phys. Fluids* **27** (1), 46–59.

FISCHER, P. F. 1997 An overlapping schwarz method for spectral element solution of the incompressible Navier–Stokes equations. *J. Comput. Phys.* **133**, 84–101.

GIANNETTI, F. & LUCHINI, P. 2007 Structural sensitivity of the first instability of the cylinder wake. *J. Fluid Mech.* **581**, 167–197.

HEALEY, J. J. 2007 Enhancing the absolute instability of a boundary layer by adding a far-away plate. *J. Fluid Mech.* **579**, 29–61.

HUERRE, P. & MONKEWITZ, P. A. 1990 Local and global instabilities in spatially developing flows. *Annu. Rev. Fluid Mech.* **22**, 473–537.

HUERRE, P. & MONKEWITZ, P. A. 2000 Open shear flow instabilities. In *Perspectives in Fluid Dynamics: a Collective Introduction to Current Research* (ed. G. K. Batchelor, H. K. Moffatt & M. G. Worster). Cambridge University Press.

HWANG, R. R. & YAO, C.-C. 1997 A numerical study of vortex shedding from a square cylinder with ground effect. *Trans. ASME: J. Fluids Engng* **119**, 512–518.

JUNIPER, M. P. 2006 The effect of confinement on the stability of planar shear flows. *J. Fluid Mech.* **565**, 171–195.

JUNIPER, M. P. 2007 The full impulse response of two-dimensional shear flows and implications for confinement. *J. Fluid Mech.* **590**, 163–185.

JUNIPER, M. P & CANDEL, S. M. 2003 The stability of ducted compound flows and consequences for the geometry of coaxial injectors. *J. Fluid Mech.* **482**, 257–269.

KIM, D.-H., YANG, K.-S. & SENDA, M. 2004 Large eddy simulation of turbulent flow past a square cylinder confined in a channel. *Comput. Fluids* **33**, 81–96.

LUNDELL, F., SÖDERBERG, L. D. & ALFREDSSON, P. H. 2011 Fluid mechanics of papermaking. *Annu. Rev. Fluid Mech.* **43**, 195–217.

MONKEWITZ, P. A., HUERRE, P. & CHOMAZ, J.-M. 1993 Global linear stability analysis of weakly non-parallel shear flows. *J. Fluid Mech.* **251**, 1–20.

PIER, B. 2002 On the frequency selection of finite-amplitude vortex shedding in the cylinder wake. *J. Fluid Mech.* **458**, 407–417.

REES, S. J. & JUNIPER, M. P. 2010 The effect of confinement on the stability of viscous planar jets and wakes. *J. Fluid Mech.* **656**, 309–336.

RICHTER, A. & NAUDASCHER, E. 1976 Fluctuating forces on a rigid circular cylinder in confined flow. *J. Fluid Mech.* **78**, 561–576.

SCHMID, P. J. 2007 Nonmodal stability theory. *Annu. Rev. Fluid Mech.* **39**, 129–162.

TAMMISOLA, O., LUNDELL, F., SCHLATTER, P., WEHRFRITZ, A. & SÖDERBERG, L. D. 2011 Global linear and nonlinear stability of viscous confined plane wakes with co-flow. *J. Fluid Mech.* **675**, 397–434.